PHYSICAL REVIEW A **97**, 023412 (2018)

Sequential double photodetachment of He$^-$ in elliptically polarized laser fields

Matthieu Génévriez,[1,*] Kevin M. Dunseath,[2] Mariko Terao-Dunseath,[2] and Xavier Urbain[1,†]
[1] *Institute of Condensed Matter and Nanosciences, Université catholique de Louvain, Louvain-la-Neuve B-1348, Belgium*
[2] *Univ Rennes, CNRS, IPR (Institut de Physique de Rennes) - UMR 6251, F-35000 Rennes, France*

(Received 27 November 2017; published 13 February 2018)

Four-photon double detachment of the helium negative ion is investigated experimentally and theoretically for photon energies where the transient helium atom is in the $1s2s\ ^3S$ or $1s2p\ ^3P^o$ states, which subsequently ionize by absorption of three photons. Ionization is enhanced by intermediate resonances, giving rise to series of peaks in the He$^+$ spectrum, which we study in detail. The He$^+$ yield is measured in the wavelength ranges from 530 to 560 nm and from 685 to 730 nm and for various polarizations of the laser light. Double detachment is treated theoretically as a sequential process, within the framework of R-matrix theory for the first step and effective Hamiltonian theory for the second step. Experimental conditions are accurately modeled, and the measured and simulated yields are in good qualitative and, in some cases, quantitative agreement. Resonances in the double detachment spectra can be attributed to well-defined Rydberg states of the transient atom. The double detachment yield exhibits a strong dependence on the laser polarization which can be related to the magnetic quantum number of the intermediate atomic state. We also investigate the possibility of nonsequential double detachment with a two-color experiment but observe no evidence for it.

DOI: 10.1103/PhysRevA.97.023412

I. INTRODUCTION

Double photodetachment, the process in which a negative ion absorbs one or several photons and ejects two electrons, has been much less studied than double photoionization, its counterpart for atoms and positive ions [1]. While the important structural differences between anions and atoms are expected to alter the dynamics of double electron ejection, experimental investigation has been hampered by the difficulty of producing anions in sufficiently high density.

Early work on double photodetachment involved moderately intense fields ($\sim 10^{10}$ W cm^{-2}) and aimed at either studying excess photon detachment, i.e., the absorption by the system of more photons than is energetically required, or at performing spectroscopy of autoionizing states embedded in the continuum [2,3]. The detection of positive ions following photodetachment is also at the basis of resonant ionization spectroscopy, although in this case the atom is optically excited to a Rydberg state and ionized by a static electric field [4]. In these studies, the production of positive ions is a means to study single photodetachment of the negative ion, and the ionization dynamics of the second electron from the neutral atom are not considered in detail. More recently, a number of studies have been devoted to double detachment in an intense field ($\geqslant 10^{13}$ W cm^{-2}), where the absence of a long-range Coulomb potential and the lower binding energy compared to atoms are expected to significantly modify the dynamics of nonsequential processes [5–10].

The work reported here concerns double detachment of the $1s2s2p\ ^4P^o$ metastable state of He$^-$ in moderately strong laser fields, with intensities comparable to those of earlier work [2,3], where multiphoton processes dominate. While no other experimental or theoretical data are available for this anion, the choice of such a few-electron system allows the physics to be studied in detail both experimentally and theoretically. For moderate intensities, the process can be treated as sequential, i.e., as single photodetachment of the anion followed by ionization of the neutral atom. The first step, shown schematically on the left-hand side of Fig. 1, involves the one-photon detachment of He$^-$; this has already been studied both experimentally and theoretically, with good overall agreement [11–13]. Detachment in the wavelength ranges from 530 to 560 nm and from 685 to 730 nm leaves helium in the $1s2s\ ^3S$ and $1s2p\ ^3P^o$ states, which can subsequently ionize by absorption of three photons, as shown on the right-hand side of Fig. 1.

It has already been shown that multiphoton ionization of excited helium atoms is greatly enhanced by resonances with higher lying states [14–17], a process known as resonance enhanced multiphoton ionization (REMPI). In a previous paper [18], we investigated three-photon ionization of He ($1s2p\ ^3P^o$), observing two-photon resonances with Rydberg states as well as an extra resonant pathway via the low-lying $1s3s\ ^3S$ state, which further complicates the ionization dynamics. Using the same experimental setup and effective Hamiltonian approach, we here extend the study reported in Ref. [18] over a wider range of photon energies and investigate the effect of different laser polarizations. The first photodetachement step is also treated in more detail.

We have shown in Ref. [18] that the magnetic quantum number M influences the double detachment dynamics since for $M = 0$, extra ionization pathways are allowed. The influence of M on double detachment in strong laser fields has also been discussed within the framework of Ammosov-Delone-Krainov- or Keldysh-like models [8,9] and was shown

---

[*] Present address: Laboratory of Physical Chemistry, ETH Zurich, CH-8093 Zurich, Switzerland.

[†] xavier.urbain@uclouvain.be

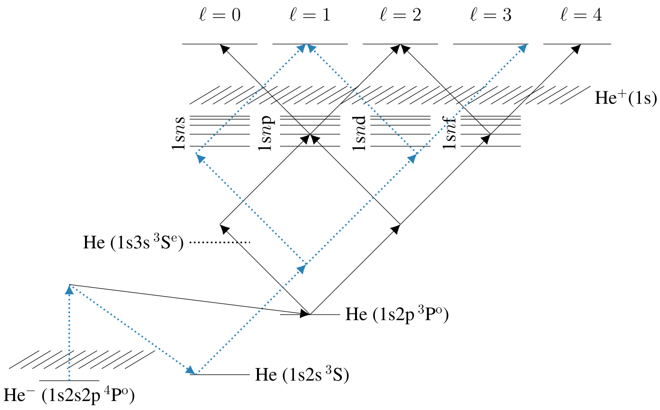

FIG. 1. Schematic energy level diagram of He$^-$ and He. The dotted arrows show the pathway responsible for double detachment of He$^-$ via the $1s2s$ intermediate state and through (2 + 1) resonance enhanced multiphoton ionization (REMPI) of the atom. The solid arrows show the pathway via the $1s2p$ state and through (1 + 1 + 1) and (2 + 1) REMPI of the atom.

to be of some importance in the saturation of the second, ionization step. This influence will also be investigated below, in particular how it depends on the wavelength and polarization of the laser light.

The paper is organized as follows: The experimental setup is briefly described in Sec. II; the R-matrix calculation for the photodetachment of He$^-$ together with the effective Hamiltonian approach used to treat ionization of helium are presented in Sec. III. Section IV presents and discusses the experimental and theoretical results.

II. EXPERIMENTAL SETUP

The experimental setup, presented in Fig. 2, is essentially the same as in Ref. [18]. We therefore give only a brief summary of its main features but describe in more detail the few modifications required for the present study.

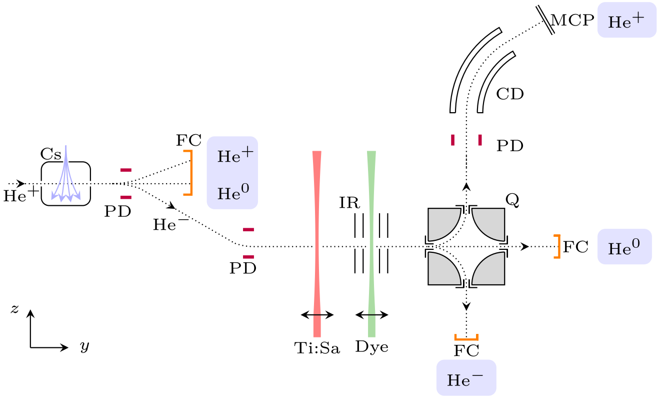

FIG. 2. Experimental setup. Cs, cesium vapor cell; PD, planar deflector; FC, Faraday cup; CD, cylindrical deflector; IR, biased interaction region; Q, quadrupolar deflector; MCP, multichannel plates; Ti:Sa, Ti:sapphire laser beam; and Dye, dye laser beam. Double arrows indicate convergent lenses. The laser beams propagate along the z direction and their polarizations, when linear, are along the y axis.

A beam of He$^+$ ions is first extracted from a duoplasmatron source, accelerated to 4 keV and mass selected by a permanent magnet. Negative helium ions He$^-$ ($1s2s2p\,^4P^o$) are produced by double charge transfer with cesium atoms in a vapor cell, with an efficiency of about 1%. Double electrostatic deflection subsequently clears the He$^-$ beam of its positive (He$^+$) and neutral (He^0) components before it enters the region of interaction with the laser beam, pumped to high vacuum ($\sim 10^{-8}$ mbar). Although He$^-$ ($1s2s2p\,^4P^o$) is metastable, the lifetimes of its $J = 1/2, 3/2$, and 5/2 fine structure components, 7.8, 12.3, and 359 μs respectively [19], are sufficiently long to perform the experiment using conventional beam transport techniques. Contamination of the beam by ground-state helium atoms due to spontaneous detachment is very weak, of the order of 1% .

The ion beam is illuminated by nanosecond laser pulses from a tunable dye laser pumped by the second or third harmonics of a Q-switched Nd:YAG laser. Coumarin 500 and pyridine 1–2 dyes were used to cover wavelength ranges from 530 to 560 nm and from 685 to 730 nm respectively. At the laser output, the pulse energy is attenuated to the required value by the combination of a $\lambda/2$ plate mounted on a high-accuracy rotation stage and a polarizing beam splitter. Laser light is then focused onto the ion beam inside the vacuum chamber by an $f = 40$ cm lens and collected, as it exits the chamber, by a pulse energy meter. The attenuation system is servocontrolled in order to maintain a constant pulse energy throughout the dye gain curve. The size of the waist at focus is about 54 μm, resulting in a peak intensity of 2.9×10^{10} W/cm^2 for 6-mJ pulses. A $\lambda/4$ plate is placed between the attenuator and the lens to change the polarization of the laser beam from linear to circular or elliptic. To avoid spurious depolarisation, no mirrors are used beyond the $\lambda/4$ plate.

Ions cross the laser spot (twice the waist) in about 250 ps, an interval much shorter than the duration of the laser pulse itself ($\sim$5 ns FWHM). During their transit, some ions undergo photodetachment and the resulting neutral atoms can further be ionized by absorbing three more photons. Beyond the interaction region, the He$^+$ ions are analyzed in energy by a quadrupolar deflector combined with a 60° cylindrical deflector and an analyzing slit, and detected by microchannel plates (MCP). The anions are collected on the other side of the quadrupole by a Faraday cup. In order to collect only those He$^+$ ions produced by photodetachment and ionization within the same dye laser pulse, a bias of 100 V is applied to the interaction region with the dye laser. He$^+$ ions produced by double detachment of He$^-$ in this region gain an energy of 200 eV while those produced by ionization of incoming He atoms gain only 100 eV. He$^+$ ions produced by collisions with the residual gas outside the interaction region gain no energy. The subsequent energy analysis performed by the quadrupolar and cylindrical deflectors readily separates the various contributions. Moreover, the detection of laser-induced He$^+$ ions is performed only in a narrow time-window centered around their time of flight from the interaction region. A second, time-shifted window is used to measure the background signal. The selection in energy and time of flight ensures quasi-background-free measurements, with less than three background counts per hundred laser shots.

In order to assess the sequential nature of the double detachment process, we have performed a two-color experiment where helium atoms are first prepared in the $1s2p$ state outside the interaction region by photodetachment by a CW Ti:sapphire laser and ionized downstream by pulses from the dye laser. By operating the tunable CW laser at a wavelength of 1005 nm, more than 99% of photodetachment occurred into He ($1s2p\,{}^3P^o$) as the cross section of this process reaches a maximum of 3.6×10^{-19} m^2 due to a resonance with the He$^-$ ($1s2p^2\,{}^4P^e$) autodetaching state [11,12]. During transit between the two laser foci, separated by less than 1 cm, 20% of the He ($1s2p\,{}^3P^o$) states decay spontaneously into He ($1s2s\,{}^3S$). By selecting downstream those ions that gained a kinetic energy of 100 eV, we could detect He$^+$ ions produced by sequential, two-color detachment and ionization only.

III. THEORY

A. Single photodetachment of He$^-$

One-photon detachment of He$^-$ has been studied in some detail over the past few decades, with particular emphasis on resonances due to doubly excited states embedded in the continuum (see the review article [1] and references therein). In the wavelength ranges spanned by the present study (530–560 nm and 685–730 nm), no such resonances are accessible and the cross section exhibits no sharp variation. Overall, there is relatively good agreement between the various theoretical and experimental results in this region [11–13,20–25]. Previous studies, however, only dealt with *linear* polarization, while the present goal is to study double detachment in an elliptically polarized field. Moreover, while partial cross sections for photodetachment into the He ($1s2s\,{}^3S$) and He ($1s2p\,{}^3P^o$) states have been considered by some authors, no data exist for partial cross sections to the various magnetic sublevels of a final state, e.g., He ($1s2p\,{}^3P^o$) with magnetic quantum numbers $M_f = 0,\pm1$. Such partial cross sections are not anecdotal since, for example, the dynamics of resonance-enhanced multiphoton ionization of He ($1s2p\,{}^3P^o$) strongly depends on M_f (see Ref. [18]). We have thus derived a formula for partial cross sections to the magnetic sublevels of a given state and calculated their values in the desired wavelength range based on reduced dipole matrix elements obtained from an R-matrix calculation.

In what follows, we assume L-S coupling and consider only dipole-allowed transitions. Since the initial state ($1s2s2p\,{}^4P^o$) has a total spin $S_i = 3/2$, the dipole selection rules impose that the residual atom is left in a triplet state. For ease of notation, we therefore do not explicitly specify the spin quantum numbers in what follows.

We consider an initial state of the unpolarized anion, denoted by $|\alpha_i L_i M_i\rangle$, where L_i is the total orbital angular momentum of the state i, M_i is its magnetic quantum number, and α_i represents all other quantum numbers required to specify the state. The residual atom is left in a state $|\alpha_f L_f M_f\rangle$ of total orbital angular momentum L_f and magnetic quantum number M_f. The ejected electron is described by continuum orbitals $|\epsilon_f \ell_f m_f\rangle$ of energy ϵ_f, orbital angular momentum ℓ_f, and magnetic quantum number m_f. The final continuum state of total angular momentum L and magnetic quantum number M, denoted by $|\alpha_f L_f \ell_f L M\rangle$, is obtained by coupling together the residual atom wave function and continuum orbitals. The length form of the partial cross section for photodetachment to a particular magnetic sublevel, averaged over the initial states and summed over the possible spin projections of the final states, is given by

$$\sigma_{\alpha_f L_f M_f}(\hat{\boldsymbol{\epsilon}}) = \frac{4\pi^2\alpha a_0^2\omega}{2L_i+1} \sum_{M_i}\sum_{L,L'} \sqrt{(2L+1)(2L'+1)} \sum_{\ell_f,m_f} \begin{pmatrix} L_f & \ell_f & L \\ M_f & m_f & -M \end{pmatrix} \begin{pmatrix} L_f & \ell_f & L' \\ M_f & m_f & -M \end{pmatrix} \times \langle \alpha_f L_f \ell_f L' M | D(\hat{\boldsymbol{\epsilon}}) | \alpha_i L_i M_i\rangle^* \, \langle \alpha_f L_f \ell_f L M | D(\hat{\boldsymbol{\epsilon}}) | \alpha_i L_i M_i\rangle\,, \tag{1}$$

which is derived from the general expression of the dipole matrix elements given by Burke [26], and where α is the fine-structure constant, a_0 is the Bohr radius, ω is the photon angular frequency, and $D(\hat{\boldsymbol{\epsilon}})$ is the dipole length operator for a given polarization vector $\hat{\boldsymbol{\epsilon}}$. In the "natural" reference frame of Tumaikin and Yudin [27,28], this is expressed as

$$\hat{\boldsymbol{\epsilon}} = \mathbf{e}_0\sqrt{\cos 2\varepsilon} - \mathbf{e}_{\pm1}\sqrt{2}\sin\varepsilon, \tag{2}$$

where $\mathbf{e}_{0,\pm1}$ are spherical unit vectors [29] and the ellipticity angle ε can take the values $-\pi/4 \leqslant \varepsilon \leqslant \pi/4$. On the right-hand side, the helicity of the vector $\mathbf{e}_{\pm1}$ corresponds to the sign of ε. The polarization is linear when $\varepsilon = 0$, left circular when $\varepsilon = \pi/4$, and right circular when $\varepsilon = -\pi/4$. The choice of reference frame is arbitrary, and a commonly used convention is to choose the quantization axis z along the electric field in the case of linear polarization, and along the direction of light propagation in the case of circular polarization. The natural frame possesses the advantage of bridging these two conventions by performing a continuous rotation of the reference frame as the ellipticity angle evolves from 0 to $\pm\pi/4$. The orientation of the reference frame in the laboratory frame thus depends on the ellipticity angle, and it is identical to standard conventions in the limiting cases of linear and circular polarization. Any other frame would yield identical results for the partial photodetachment cross sections, keeping in mind that the M values are projections of the angular momentum along the quantization axis, and an appropriate rotation must therefore be performed in order to make meaningful comparisons.

With the definition (2) for the polarization vector, the dipole matrix elements appearing in (1) can be obtained from the reduced matrix elements $(\alpha_f L_f \ell_f L||\boldsymbol{D}||\alpha_i L_i)$ using the

Wigner-Eckart theorem [29]:

$$\begin{aligned}&\langle\alpha_f L_f \ell_f L M|\, D(\hat{\boldsymbol{\epsilon}})\, |\alpha_i L_i M_i\rangle\\ &= (-1)^{-L-M}\left[\begin{pmatrix} L & 1 & L_i \\ -M & 0 & M_i \end{pmatrix}\sqrt{\cos 2\varepsilon} - \begin{pmatrix} L & 1 & L_i \\ -M & \pm 1 & M_i \end{pmatrix}\sqrt{2}\sin\varepsilon\right](\alpha_f L_f \ell_f L||\boldsymbol{D}||\alpha_i L_i), \qquad (3)\end{aligned}$$

where $\boldsymbol{D}$ is the tensor operator corresponding to $D(\hat{\boldsymbol{\epsilon}})$. Note that the reduced matrix element does *not* depend on the polarization.

The cumulated photodetachment probability to a particular final state $|\alpha_f L_f M_f\rangle$ is readily obtained from the partial cross sections by solving the rate equation $dN(t)/dt = -\sigma\phi(t)N(t)$ with appropriate boundary conditions,

$$P_{L_f M_f}(t) = \frac{\sigma_{\alpha_f L_f M_f}}{\sigma}\left[1 - e^{-\int_{-\infty}^{t} dT \sigma\phi(T)}\right], \qquad (4)$$

where $\phi(T)$ is the instantaneous photon flux and the total cross section σ is obtained by summing the partial cross sections over all quantum numbers. Note that the intensity, or photon flux, required for double detachment is very high and therefore, in the region where it occurs, the exponential term on the right-hand side of the above equation is essentially zero; i.e., photodetachment is saturated.

In order to compute the partial cross sections (1), (3) and hence the cumulated photodetachment probability, we require the reduced dipole matrix elements $(\alpha_f L_f \ell_f L||\boldsymbol{D}||\alpha_i L_i)$, which are independent of the polarization. In the work reported here, these were obtained from a standard R-matrix calculation including the five lowest triplet states of helium ($1s2s\,^3S$, $1s2p\,^3P^o$, $1s3s\,^3S$, $1s3p\,^3P^o$, $1s3d\,^3D$), using the UK APAP (atomic processes for astrophysical plasmas) suite of computer codes [30]. Details are given in the Appendix.

B. Three-photon ionization of He

After the first electron is ejected from He$^-$, and as the neutral atom moves forward through the laser pulse, the intensity rises. If the photon energy is appropriately chosen, the intensity may become sufficiently high to favor the $(1+1+1)$ or $(2+1)$ REMPI of the atom. In Ref. [18], we have shown that effective Hamiltonian (EH) theory can provide an accurate description of the phenomenon and hence can be used to model the experiment in detail. EH theory has been described in some length elsewhere [31–33], so we shall only briefly summarize it here, concentrating on the details relevant to the present study.

In EH theory, Hilbert space is partitioned into two different subspaces: the model space $\mathscr{P}$ contains the quasiresonant bound states, and its orthogonal complement $\mathscr{Q}$ spans the rest of Hilbert space. The effective Hamiltonian is built from the exact Hamiltonian of the $\mathscr{P}$ space, while the $\mathscr{Q}$ space is included through additional, perturbative matrix elements coupling model-space states. In this respect, EH theory can be considered as a semiperturbative treatment of multiphoton ionization. Choice of the $\mathscr{P}$ space is critical since it must be small enough so that the effective Hamiltonian matrix is kept small and calculations are relatively simple, and yet contain all states essential for the REMPI dynamics.

The effective Hamiltonian H_{eff} satisfies the following eigenvalue equation:

$$H_{\text{eff}}\,|\psi_p\rangle = E\,|\psi_p\rangle\,, \qquad (5)$$

where $|\psi_p\rangle$ is the model space wave function. Each eigenvalue can be written as $E = E_0 + \Delta - \mathrm{i}\frac{\Gamma}{2}$, the real part being the Stark-shifted energy of the field-dressed atomic state and Γ its total ionization width. The effective Hamiltonian valid up to the second order of perturbation theory is

$$H_{\text{eff}} = PH_0P + PVP + P\left(S + \Omega - \mathrm{i}\frac{\Gamma}{2}\right)P, \qquad (6)$$

where V is the exact atom-field interaction operator and H_0 is the exact "free" Hamiltonian, containing the field-free atomic and light-field Hamiltonians. P is the Feshbach projection operator, projecting the wave function onto $\mathscr{P}$-space states: $\sum_{i\in\mathscr{P}} |i\rangle\langle i|$. The operator S is a two-photon transition operator connecting the $\mathscr{P}$-space states via nonresonant bound states and the operators Ω and Γ represent two-photon couplings between model-space states through the ionization continua (see Ref. [18] for the detailed expression of these operators).

The eigenvalues of H_0 for bound states are $E_i = \mathcal{E}_i - N\omega$, where $\mathcal{E}_i$ is the field-free energy of the bound state and N is the number of photons absorbed. Field-free energies for low-lying bound states ($n \leqslant 3$) are taken from the NIST atomic database [34]. The energies of Rydberg states are computed from their principal quantum number n and quantum defect $\delta_{n\ell}$. The latter is calculated using Ritz's expansion with coefficients given by Drake [35]. By convention, $N = 0$ for either of the $1s2s$ or $1s2p$ initial states, $N = 1$ for the $1s3s$ and $1s3d$ states and $N = 2$ for the Rydberg states. The eigenvalues of the continuum states of H_0 are, similarly, $e = \epsilon_f - 3\omega$, where ϵ_f is the photoelectron energy.

The one- and two-photon matrix elements (V_{ij}, S_{ij}, Ω_{ij}, and Γ_{ij}) coupling states of the model space are expressed within the dipole and rotating-wave approximations [36], justified by the moderate laser intensities and the explicit treatment of only quasiresonant bound states. Their calculation for all polarization states $\hat{\boldsymbol{\epsilon}}$ is prohibitive, but can be greatly simplified, as for the photodetachment of He$^-$, by virtue of the Wigner-Eckart theorem. Reduced matrix elements, independent of $\hat{\boldsymbol{\epsilon}}$, are calculated only once using (i) two-electron DVR basis functions for couplings between low-lying states and (ii) quantum defect wave functions for couplings among Rydberg states and between Rydberg and continuum states (see Ref. [18]). Dipole matrix elements for any, arbitrary $\hat{\boldsymbol{\epsilon}}$ are then readily calculated using Eq. (3) and the effective Hamiltonian matrix is then constructed using these elements.

We have built two effective Hamiltonians to describe the REMPI of the $1s2s$ and $1s2p$ initial states respectively. For the $1s2s$ state, ionization proceeds via a two-photon resonance with the Rydberg $1sns$ and $1snd$ states. The model space includes the $1s2s$, $1sns$, and $1snd$ states with n in the range from 4 to 27, and the wave function is expressed as

$$|\psi_p(t)\rangle = c_{2s0}(t)\,|2s0\rangle + \sum_{n=4}^{27}\left[c_{ns0}(t)\,|ns0\rangle + \sum_M c_{ndM}(t)\,|ndM\rangle\right]. \quad (7)$$

The $1s$ orbital has been omitted in the $|n\ell M\rangle$ basis vectors for brevity. The total orbital angular momentum L has also been omitted and is equal to that of the outer electron ($L = \ell$). The summation over the total magnetic quantum number M runs from $-\ell$ to $+\ell$ for each basis vector. For the $1s2p$ state, ionization proceeds through the $(1+1+1)$ and $(2+1)$ REMPI schemes shown in Fig. 1. The model space is thus spanned by one of the magnetic sublevels of the $1s2p$ state, defined by its magnetic quantum number M_f, and the $1s3s$, $1s3d$, $1snp$, and $1snf$ states. The wave function is given by

$$|\psi_p(t)\rangle = c_{2pM_f}(t)\,|2pM_f\rangle + c_{3s0}(t)\,|3s0\rangle + \sum_M \left\{ c_{3dM}(t)\,|3dM\rangle + \sum_{n=6}^{45}[c_{npM}(t)\,|npM\rangle + c_{nfM}(t)\,|nfM\rangle]\right\}. \quad (8)$$

For both initial states, the $\mathscr{Q}$ space is truncated to a finite size and includes only the bound and continuum states involved in two-photon couplings between $\mathscr{P}$-space states. It comprises bound states up to $n = 70$ and continuum states up to energies where bound-free couplings are negligible. For linear polarizaton, selection rules ($\Delta M = 0$) permit only those states with the same magnetic quantum number as the initial state to be populated. This in turn keeps the size of the effective Hamiltonian small, e.g., 83×83 for the $1s2p$ initial state. In the general case of elliptic polarization, looser selection rules ($\Delta M = 0,\pm1$) yield a significantly larger effective Hamiltonian, with a size up to 409×409 for the $1s2p$ state.

Once the effective Hamiltonian is constructed, it is used to propagate the wave function along the atom's trajectory through the laser pulse. This is done by solving the time-dependent Schrödinger equation [37], whose formal solution may be written as

$$|\psi_p(t+\Delta t)\rangle = e^{-iH_{\mathrm{eff}}(t)\Delta t}\,|\psi_p(t)\rangle\,. \quad (9)$$

The wave function is iteratively propagated by computing numerically the matrix exponential $e^{-iH\Delta t}$ with the EXPOKIT computer package [38]. The time dependence of the effective Hamiltonian arises from the dependence of the couplings between model-space states on the intensity of the laser field, itself evolving in time as the atom travels through the laser focus. The wave function is propagated up to about $t = 4 \times 10^7$ a.u. in steps of $\Delta t \simeq 10^4$ a.u. The initial condition for propagation starting from the He ($1s2s\,^3S$) state is

$$|c_{2s0}(0)|^2 = P_{2s0}(t \to \infty), \quad (10)$$

where $P_{2s,0}$ is the detachment probability, given by Eq. (4). All other coefficients are zero. Similarly, the initial condition for the He ($1s2p\,^3P^o$) state is given by

$$\left|c_{2pM_f}(0)\right|^2 = P_{2pM_f}(t \to \infty), \quad (11)$$

and all other coefficients are zero. Such initial conditions imply that the photodetachment and ionization processes are sequential and that the former occurs well before the latter, i.e., at much lower intensities. Because of the non-Hermiticity of the effective Hamiltonian, the norm of the wave function at the end of the propagation has decreased by an amount p. This quantity corresponds to the probability of ejecting two electrons from the He$^-$ ion via either the He ($1s2s\,^3S$) state or one of the magnetic sublevels of the He ($1s2p\,^3P^o$) state. The total ejection probability p_{tot} is the sum over all channels. Note that for each photon energy, p_{tot} is computed for a range of peak intensities and appropriate averaging over the ion beam section and integration over the pulse duration is subsequently performed in order to simulate experimental conditions (see Ref. [18]). Simulated results are also multiplied by 0.56 to account for the MCP detection efficiency.

IV. RESULTS AND DISCUSSION

A. Single photodetachment

We have studied the one-photon, single detachment of He$^-$ under elliptical polarization and in the wavelength range from 685 to 730 nm (1.698 to 1.810 eV). Branching ratios to He ($1s2s\,^3S$) and He ($1s2p\,^3P^o$, $M_f = 0,\pm1$) final states were calculated using Eq. (1) with reduced dipole matrix elements obtained from the R-matrix calculation described in the Appendix. This calculation yielded an electron affinity of 75.5 meV, which compares favorably with the experimental value of 77.516 meV [39]. The total and partial cross sections are in good agreement with those of an earlier R-matrix calculation [11].

The branching ratios are in fact only weakly dependent on the wavelength. A representative set is shown in Fig. 3, for different light polarizations at $\lambda = 690$ nm (1.797 eV). The population of the $1s2s$ state ($R_{2\mathrm{s}} = 0.66$) is nearly twice that of the $1s2p$ state ($R_{2\mathrm{p}} = 0.34$), and this sharing is independent of the ellipticity. The $1s2p$ state is slightly less populated at shorter wavelengths ($R_{2\mathrm{p}} = 0.33$ for $\lambda = 685$ nm) and slightly more populated at longer wavelengths ($R_{2\mathrm{p}} = 0.39$ for $\lambda = 730$ nm).

The branching ratio to the $1s2s$ state with a single, isotropic sublevel $M_f = 0$ does not depend on the ellipticity. The $1s2p$ state has three magnetic sublevels with $M_f = 0,\pm1$. The branching ratio for $M_f = 1$ and $M_f = -1$ respectively increases and decreases slightly as the ellipticity angle goes from 0 to $\pi/4$. The branching ratio for $M_f = 0$ is essentially independent of ellipticity, with only a slight (5%) increase between linear and circular polarization. For linear polarization ($\varepsilon = 0$), the three sublevels are almost equally populated, with 34% in each of the $M_f = 1$ and -1 states and 32% in the $M_f = 0$ state. For left circular polarization σ^+ ($\varepsilon = \pi/4$), the $M_f = 1$ state is preferentially populated with 39% of the total $1s2p$ population, compared to 34% in $M_f = 0$ and 27% in

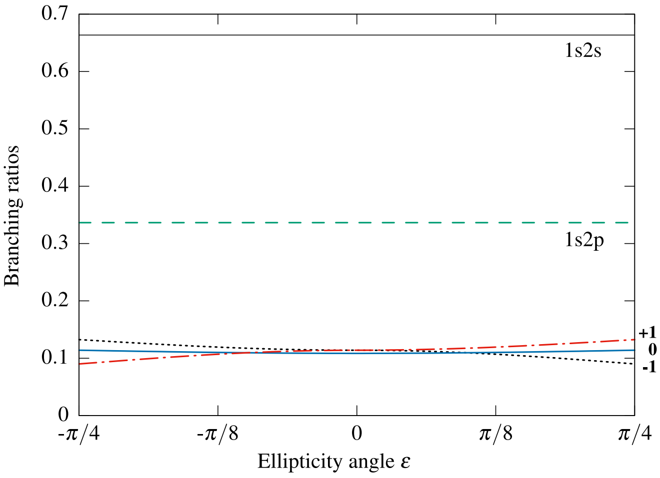

FIG. 3. Branching ratios $R_{2s,2p}$ for the photodetachment of He$^-$ into the He ($1s2s\,^3S$) and He ($1s2p\,^3P^o$) states at $\lambda = 690$ nm. Full thin line, $1s2s$ state; dashed line, $1s2p$ state. Branching ratios to the various magnetic sublevels of the $1s2p$ state are also shown, and corresponding M_f values are labeled on the right-hand side of the graph. Dotted line, $M_f = -1$; full thick line, $M_f = 0$; dash-dotted line, $M_f = +1$.

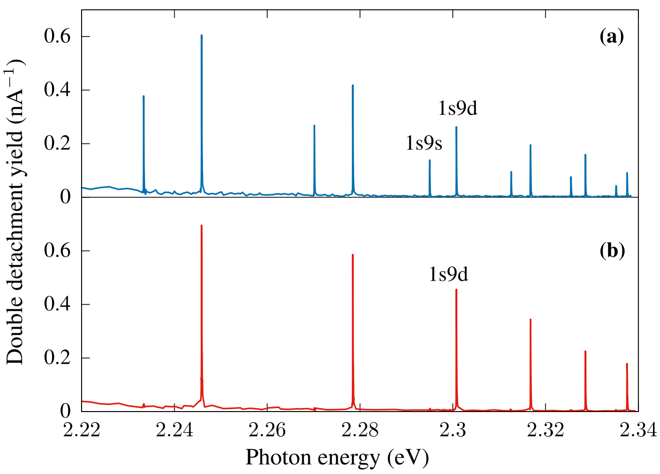

FIG. 4. Experimental double detachment spectrum as a function of the photon energy. Top graph (a), linear polarization. Bottom graph (b), left circular polarization. Data shown are the number of He$^+$ ions produced by a 6-mJ laser pulse and for a He$^-$ beam of 1 nA.

$M_f = -1$. This may be expected since the dipole transition selection rule is $\Delta M = +1$. For right circular polarization σ^- ($\varepsilon = -\pi/4$), the opposite behavior is observed with the $M_f = -1$ state being more populated.

The branching ratios to the various magnetic sublevels of the $1s2p$ state depend on the choice of the reference frame, since M_f values represent the projection of the orbital angular momentum onto the quantization axis z. In the natural reference frame, the polarization vector given by Eq. (2) rotates in the laboratory frame with the ellipticity angle, so that magnetic quantum numbers for different polarizations correspond to projections onto quantization axes with different orientations. Such dependence, however, does not affect the final conclusions since all calculations to determine measurable quantities are performed within the same frame, and the final results are summed over all M_f values, i.e., all orientations, before being compared to experiment. As noted in the previous section, for linear ($\varepsilon = 0$) and circular ($\varepsilon = \pm\pi/4$) polarizations, the natural frame coincides with the standard choice of reference frame and comparisons with other data are straightforward. Moreover, calculations within other reference frames would yield results equivalent to the present ones and which can be compared to one another after appropriate rotation by means of Wigner D matrices [29].

We note that in Ref. [18], a population distribution of (0.25, 0.5, 0.25) was assumed for the (−1, 0, 1) magnetic sublevels of the $1s2p$ state for linear polarization, as it provided the best fit to some of the experimental results. The present calculation proves this assumption incorrect and, while it does not modify the conclusions drawn in Ref. [18], it changes to some extent the relative height of the $1snp$ and $1snf$ peaks in the simulated He$^+$ ion spectra.

The behavior of the branching ratios for magnetic sublevels is established here for photodetachment of He$^-$, but the trends observed most certainly hold for other anions. The magnitude of the photodetachment cross section depends on the reduced dipole matrix elements, but their dependence on magnetic number M_f and polarization $\hat{\boldsymbol{\epsilon}}$ derives from angular momentum algebra. Relatively small variations between different anions or final states are expected to arise since matrix elements and geometrical factors are entangled in the various summations of Eq. (1).

B. Double photodetachment

1. Transient He($1s2s\,^3S$) state

We first consider double detachment in the photon energy range between 2.22 and 2.34 eV, corresponding to the wavelength region from 530 to 560 nm covered by the laser when supplied with coumarin 500 dye. Inspection of the helium triplet spectrum indicates that the three-photon ionization of He ($1s2s\,^3S$) is strongly enhanced by two-photon resonances with Rydberg $1sns$ and $1snd$ states, as shown in Fig. 1, while the two-photon ionization of He ($1s2p\,^3P^o$) is nonresonant. One may thus expect double detachment to proceed preferentially through the $1s2s$ intermediate state, even though the number of photons required is higher than for the $1s2p$ state. This hypothesis is supported by the experimental spectrum for linear polarization, shown in Fig. 4(a). The spectrum represents the number of He$^+$ ions, created from an incoming He$^-$ beam of 1 nA by a 6-mJ laser pulse, as a function of the photon energy. The two series of peaks correspond to two-photon excitation from $1s2s$ to respectively $1sns$ and $1snd$ states with $n = 7$ to $n = 12$, which are subsequently ionized by another photon. In the present wavelength range, double photodetachment therefore occurs by photodetachment and (2 + 1) REMPI of He ($1s2s\,^3S$). Ionization from higher Rydberg levels, with n up to 115, has been studied by Wall *et al.* [40] using a two-photon laser excitation and static field ionization scheme. In the low photon energy range, a continuous, slowly rising background is observed. It can be attributed to the onset of the (1 + 1) REMPI of the $1s2p$ state through a one-photon resonance with the $1s3d$ state, located at $\lambda = 587.7$ nm (2.110 eV). Although we are still far de-

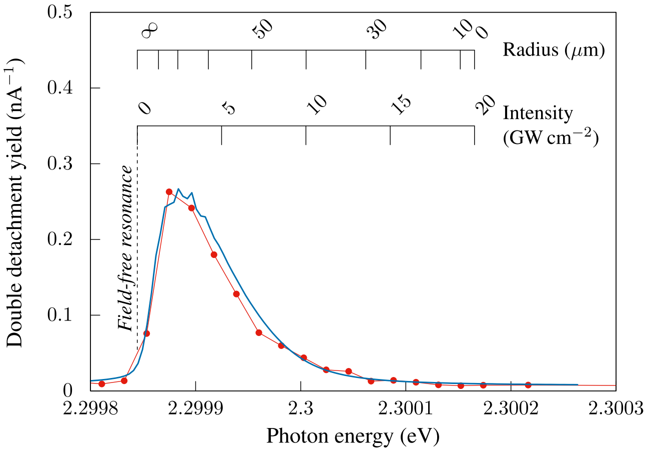

FIG. 5. Details of the $1s9d$ peak in the double detachment spectrum. Full circles, experiment; full line, simulation. Data are for linear polarization and 6-mJ laser pulses. The vertical dotted line indicates the position of the field-free $1s2s$-$1s9d$ two-photon resonance. For larger photon energies, the $1s2s$ energy is Stark shifted and resonance condition is met for different laser intensities, as indicated by the intensity scale. A given intensity corresponds to a particular radius with respect to the center of the laser profile, as indicated by the radius scale. This radius defines an effective interaction cylinder, within which production of He$^+$ can occur.

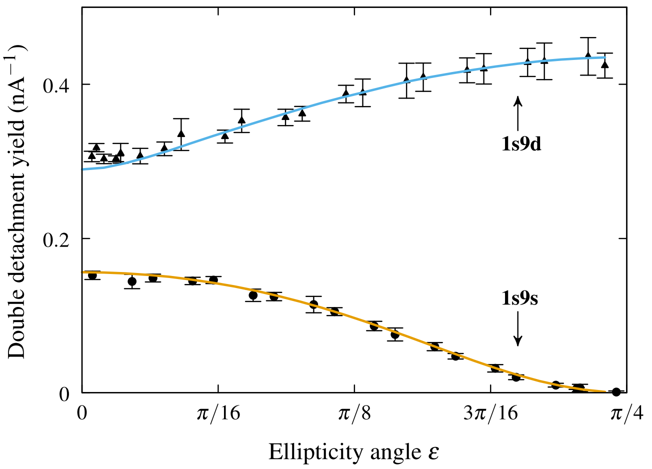

FIG. 6. Experimental and simulated double detachment yield as a function of the ellipticity angle. Triangles are experimental data for $\lambda = 539.08$ nm and correspond to resonance with the Rydberg $1s9d$ state. Circles are experimental data for $\lambda = 540.43$ nm and correspond to resonance with the Rydberg $1s9s$ state. Both full lines are the result of simulations for the same wavelengths, and have been scaled by 0.8 and 1.02 for the $1s9d$ and $1s9s$ states respectively.

tuned from this resonance, the contribution of this two-photon process to the double detachment yield is non-negligible compared to the three-photon process examined here.

The detailed profile of the peaks in the double detachment spectrum, for example, that corresponding to the $1s2s$-$1s9d$ resonance shown in Fig. 5, provides additional information on the ionization dynamics. Note that in this case the simulation was performed for a 68-μm laser waist in order to match the width of the experimental peak. No vertical scaling was applied to the simulated data. The size of the waist has not been measured for the present wavelength range (around 539 nm) and deviations from the 54-μm waist measured for the range from 685 to 730 nm are considered possible. The width of the peak is much larger than the laser bandwidth of 0.05 cm^{-1} (6.2 μeV), and it is asymmetrical, with a pronounced spread toward higher photon energies. Processes leading to this type of profile are threefold, and have been partly discussed in Ref. [18] and by other authors [40]. We first note that the $1s2s$ state is shifted down in energy for increasing laser intensities by the AC Stark shift, while the Rydberg series remain essentially unperturbed. Therefore, even if the laser is blue detuned from the $1s2s$-$1s9d$ resonance, the increasing intensity experienced by the helium atom moving through the laser focus will *dynamically* bring the $1s2s$ state into resonance with the $1s9d$ state, where population transfer occurs. As the laser is further blue detuned, the exact resonance condition is met at increasing intensities, until the value required exceeds the laser peak intensity. Assuming a Gaussian laser profile, the intensity at which resonance occurs corresponds to a specific radius with respect to the center of the profile, and thus defines a certain interaction cylinder, within which production of He$^+$ can occur. The volume of this cylinder shrinks as detuning becomes larger, consequently decreasing the He$^+$ signal. Finally, close to a zero-field resonance, population transfer to the Rydberg state occurs early on as the atom crosses the laser focus. Therefore, the duration of the interaction between the Rydberg state and the laser field is long and the ionization probability high. Blue detuning results in delayed population transfer, reduced interaction time, and therefore reduced ionization probability, also resulting in a drop in the He$^+$ yield.

Turning to circular polarization, Fig. 4(b) provides a particularly illustrative example of dipole selection rules. In the case of left circular polarization (σ^+), selection rules for a two-photon transition give $\Delta M = +2$. Excitation from the $1s2s$ state to a Rydberg $1sns$ state is therefore forbidden, and the $1sns$ peak in the He$^+$ spectrum disappears. The same argument applies in the case of right circular polarization (σ^-), for which the selection rule is $\Delta M = -2$, hence leading to the same spectrum.

The evolution of double detachment as the polarization is tuned from linear to left circular is shown in Fig. 6. Measurements were performed both for the $1s2s$-$1s9d$ and $1s2s$-$1s9s$ resonances, corresponding to photon energies of 2.2999 and 2.2942 eV, respectively, by stepwise rotation of the $\lambda/4$ plate while recording the corresponding He$^+$ signal. The effective Hamiltonian approach was used to simulate the experiment for the same photon energies, and the final results are scaled by 0.8 and 1.02 respectively in order to best fit the experimental values. We first note that the shape of the simulation curves follow the experimental data very well. The $1s9d$ peak amplitude increases as the polarization gets closer to circular, a fact that can be attributed to increasing coupling strength and ionization rate. For example, inspection of the value of the matrix element coupling the $1s2s$ state to the $1s9d$ state shows that, while the reduced matrix elements are identical, geometrical factors arising from the polarization result in a coupling that is a factor 1.5 larger for circular polarization than for linear polarization. In sharp contrast, the

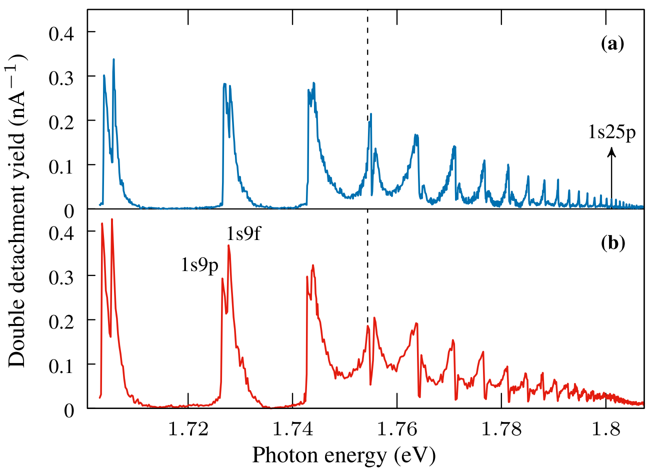

FIG. 7. Double detachment spectrum as a function of the photon energy. Top graph (a), linear polarization. Bottom graph (b), left circular polarization. The vertical dashed lines indicate the position of the $1s2p$-$1s3s$ resonance. Resonances with Rydberg states are observed up to $n = 35$. The laser pulse energy is 6 mJ.

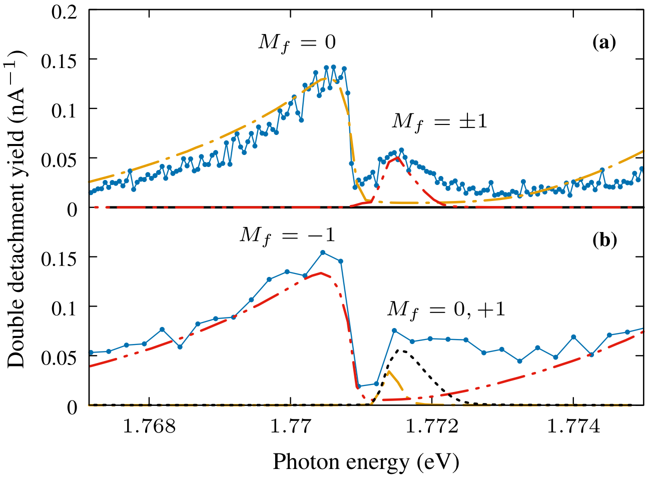

FIG. 8. Details of the double detachment spectrum around the $1s2p$-$1s13p$ (left peak) and $1s2p$-$1s13f$ (right peak) resonances. Top graph (a), linear polarization; bottom graph (b), left circular polarization. Full circles, experimental data; dash-dot-dot line, simulated $M_f = -1$ contribution; dash-dot line, simulated $M_f = 0$ contribution; dotted line, simulated $M_f = +1$ contribution. For linear polarization, $M_f = +1$ and $M_f = -1$ contributions are identical; therefore only twice the $M_f = -1$ contribution is shown. All simulated contributions are scaled by 0.45.

amplitude of the $1s9s$ peak drops to zero as the polarization becomes circular, a direct result of the dipole selection rules.

2. Transient He(1s2p $^3P^o$) state

The double detachment of He$^-$ for photon energies around 1.76 eV also exhibits resonance series, as can be seen in the experimental spectra shown in Fig 7. The spectrum for linear polarization has already been studied in Ref. [18], so we shall only recall the most important features before investigating the influence of the laser polarization. In the present photon energy region, photodetachment leaves helium in its $1s2s\,^3S$ and $1s2p\,^3P^o$ states, and three-photon ionization of the latter is enhanced due to two-photon resonances with Rydberg $1snp$ and $1snf$ states. The shape of the spectrum is, however, very different from that presented in Fig. 4 due to the presence of additional, one-photon resonances between the $1s2p$ and $1s3s$ states and the $1s3s$ and $1snp$ states. Ionization proceeds either through $(1+1+1)$ REMPI via the $1s3s$ state and a Rydberg $1snp$ state, or through $(2+1)$ REMPI preferentially via a $1snf$ Rydberg state. In linear polarization, the magnetic sublevel of $1s2p$ with $M_f = 0$ ionizes through the $(1+1+1)$ scheme while those with $M_f = \pm1$, which cannot couple to the $1s3s$ state, preferentially do so through the $(2+1)$ scheme.

In the detailed peak profiles presented in Fig. 8(a), the rightmost peak, corresponding to a $1snf$ resonance, exhibits the same spread toward higher photon energies observed for the He($1s2s\,^3S$) transient state, which can be attributed to the same dynamical processes. The leftmost peak, corresponding to $1snp$ resonances, spreads instead toward lower photon energies, indicating that the $1s2p$ state is shifted up in energy. The spread, however, changes direction toward higher photon energies below the $1s2p$-$1s3s$ resonance (see Fig. 7). This spreading and its reversal can be explained by the strong AC Stark shift of the $1s2p$ state due to the $1s3s$ state, which has opposite signs on either side of the resonance [18].

We next investigate the effect of polarization on the double detachment dynamics, and in particular on the respective contributions of the various magnetic sublevels of the $1s2p$ state. The detailed spectrum corresponding to resonances with $n = 13$ states is shown in Fig. 8, along with the simulated contributions from the $M_f = 0,\pm1$ magnetic sublevels. The most important difference between linear and circular polarization is the change of shape of the $M_f = 0$ and $M_f = -1$ contributions to the He$^+$ yield. For linear polarization, selection rules allow the $1s2p$ ($M_f = 0$) state to couple to the $1s3s$ state, which itself couples to the $1s13p$ state, thus yielding a peak that is both broad, because of the strong AC Stark shift of the $1s2p$ state, and intense, due to the large enhancement of ionization by the $(1+1+1)$ channel. In the case of left circular polarization, coupling to the $1s3s$ state becomes allowed for the $M_f = -1$ magnetic sublevel, and the contributions of the various magnetic sublevels change accordingly. Therefore, the attribution of the $1snp$ peaks to $M_f = 0$ and the $1snf$ peaks to $M_f = \pm1$ for linear polarization changes to $M_f = -1$ and $M_f = 0,1$ respectively for left circular polarization and to $M_f = 1$ and $M_f = -1,0$ for right circular polarization. As a result, by carefully tuning the laser wavelength and polarization, it is possible to address a specific magnetic sublevel of the initial state of the transient atom.

Apart from the changes in the different M_f contributions, other differences in the shape of the peaks can be observed between the double detachment spectra for circular and linear polarization, in particular on the high photon energy side (see Figs. 7 and 8). These arise from two different effects and differ for the $1snp$ and $1snf$ peaks. Let us first consider the $1snp$ peaks. Because of changes in the geometrical factors, the nonresonant AC Stark shift of the $1s2p$ ($M_f = -1$) sublevel for circular polarization is smaller than that of the $1s2p$ ($M_f = 0$) sublevel for linear polarization. Hence, since Rydberg series are unperturbed and the downward shift of the $1s2p$ energy is smaller, the peaks will spread less toward higher photon energies. However, above the $1s2p$-$1s3s$ resonance, the $1s2p$ state will be significantly shifted upward in energy due to its interaction with the $1s3s$ state. The spread of the $1snp$ peak is therefore the result of a competition between the nonresonant and resonant AC Stark shifts, so that a smaller nonresonant contribution leads to an increased upward shift, and therefore an increased spread toward lower photon energies. In Fig. 8, the intensity of the $1snp$ peak is essentially the same for linear and circular polarization. Although the ionization rate of the $1snp$ states is 16% higher for circular polarization, this increase is compensated by the lower (19%) population of the $M_f = -1$ sublevel for circular polarization compared to that of the $M_f = 0$ sublevel for linear polarization.

Let us now consider the $1snf$ peak. For linear polarization, contributions from $M_f = -1$ and $M_f = +1$ are strictly equivalent. This is no longer true in the case of circular polarization, and the $M_f = +1$ sublevel gives the dominant contribution while that for $M_f = 0$ is very similar to those for $M_f = \pm 1$ in the case of linear polarization. Investigating changes in matrix elements due to modified geometrical factors shows that the AC Stark shift of the $1s2p$ $(M_f = 0)$ sublevel for circular polarization is identical to that of the $1s2p$ $(M_f = \pm 1)$ sublevels for linear polarization, while that of the $1s2p$ $(M_f = 1)$ sublevel is twice larger. Matrix elements coupling the $1s2p$ state with $M_f = 1$ to Rydberg $1snf$ states are also significantly larger for circular polarization. Finally, the $M_f = 1$ sublevel is slightly more populated by photodetachment in circular polarization. Such increases explain why the $1snf$ peak becomes larger and significantly broadens when switching from linear to circular polarization.

Discrepancies between experimental and simulated yields, as observed in Fig. 8, may be due to variations in the transmission of the He^+ ions to the detector, slightly imperfect circular polarization of the laser light, imperfect modeling of the experimental conditions and inaccuracies in the effective Hamiltonian matrix elements.

Finally, the evolution of the double detachment yield as a function of the light polarization is shown in Fig. 9. The experimental yield was measured for a photon energy of 1.767 eV, chosen to probe the minimum between the $1s2p$-$1s12f$ and $1s2p$-$1s13p$ resonances, where the influence of the polarization is most prominent. Simulations were also performed at the minimum, which in the calculations is located at a slightly lower photon energy (1.766 eV). The double detachment signal comes mainly from the $1s2p$-$1s13p$ resonance, with the contributions of the various magnetic sublevels evolving from predominantly $M_f = 0$ to mostly $M_f = -1$. The onset of the contribution from $M_f = +1$ as the polarization becomes more circular is reminiscent of the broadening and increase in magnitude of the $1s2p$-$1snf$ peaks discussed above, with $n = 12$ here.

3. *Sequential* versus *nonsequential*

The above treatment considers photodetachment and REMPI as sequential events. Given the satisfactory agreement between simulated and measured ion yields, this appears reasonable. Detachment is indeed very efficient and occurs at low intensity, i.e., early in the pulse. The onset of REMPI requires much higher intensities and occurs later, when detachment is fully saturated. One possible exception is when the photon energy is tuned close to the $1s2p$-$1s3s$ resonance at 707 nm, since population transfer to the Rydberg states via the $1s3s$ state can take place very early in the pulse, at lower intensities where photodetachment is not yet saturated.

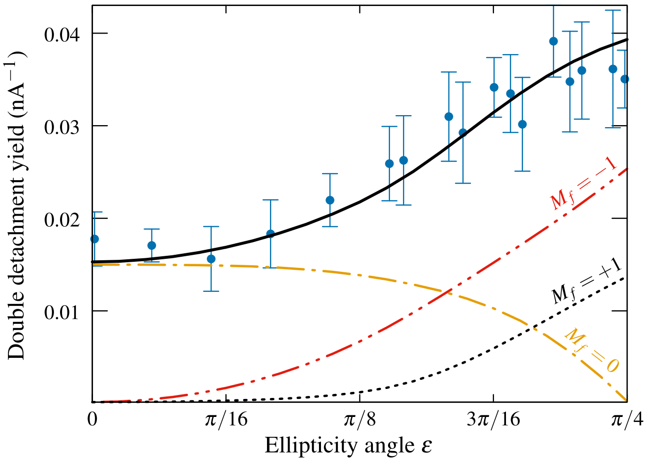

FIG. 9. Experimental and simulated double detachment yield as a function of the ellipticity angle, at the photon energy corresponding to the minimum between the $1s2p$-$1s12f$ and $1s2p$-$1s13p$ resonances. Full circles, experimental yield; full line, simulated yield; dash-dot-dot line, $M_f = -1$ contribution; dash-dot line, $M_f = 0$ contribution; dotted line, $M_f = +1$ contribution. The experimental yield is for a photon energy of 1.767 eV (701.72 nm) and the simulated one for 1.766 eV (702.05 nm). Simulated yields are scaled by 0.65 to match experimental values. The laser pulse energy is 6 mJ.

In order to establish the sequential nature of the double detachment process close the $1s2p$-$1s3s$ resonance, we have performed a two-color experiment where helium atoms are first prepared in the $1s2p$ state by photodetachment by a CW laser tuned to $\lambda = 1005$ nm, and subsequently ionized downstream by the second, pulsed dye laser used previously. The two laser beams are spatially separated, and we select those He^+ ions that result from photodetachment by the first laser followed by multiphoton ionization by the second.

The resulting double detachment spectrum is shown in Fig. 10 and compared with the one-laser spectrum, where detachment and ionization occur within the same laser pulse. Since the first laser in the two-color experiment is less efficient in producing helium atoms, the measured yield is smaller and was scaled in Fig. 10 in order to directly compare with the one-color spectrum. No significant differences can be seen, suggesting that no strong nonsequential processes occur. The experiment was run for linear polarization and we have also observed that when the two laser polarizations are parallel or perpendicular, essentially the same spectra are obtained, to within experimental error bars.

The absence of any nonsequential process is not surprising considering the moderate laser intensities in our experiments (of the order of $10^{10}\ \mathrm{W/cm^2}$). The dominant mechanism for nonsequential double ionization is the recollision of the first photoelectron with the residual atom or ion. The laser intensity required for this process can be estimated using the semiclassical recollision model [41,42]. For wavelengths

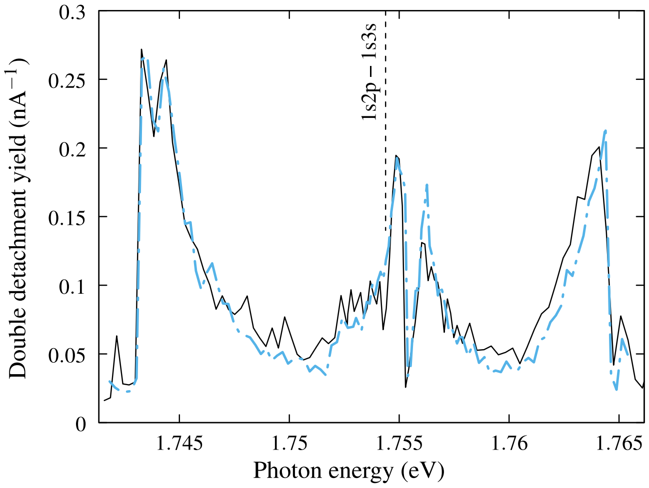

FIG. 10. Double detachment spectrum around the $1s2p$-$1s3s$ resonance. Dot-dashed line, two-color, sequential measurement, multiplied by 35; full line, one-color measurement. The vertical dotted line indicates the exact position of the $1s2p$-$1s3s$ resonance. The laser pulse energy is 6 mJ.

around 707 nm corresponding to the $1s2p$-$1s3s$ resonance, intensities of over 8×10^{11} W/cm^2 would be necessary in order to eject the $11p$ electron. Coulomb focusing, which can greatly enhance the nonsequential double ionization rate of atoms and multiply charged ions [43], does not occur here since the recollision is with a neutral atom.

V. CONCLUSION

We have reported a joint experimental and theoretical investigation of the double detachment of He$^-$ in moderately strong laser fields, for wavelengths ranging from 530 to 560 nm and from 685 to 730 nm, for various polarizations of the laser light. The experiment relies on counting He$^+$ ions, produced from a He$^-$ beam by 6-mJ laser pulses, as a function of the wavelength and ellipticity angle. The theoretical work treats double detachment in two sequential steps. The single detachment step is studied within an R matrix approach by calculating branching ratios into the various final atomic states and their magnetic sublevels for arbitrary elliptical polarization. Subsequent ionization of the neutral atom is studied using effective Hamiltonian models designed to account for all possible polarizations. They allow lightweight calculations which reproduce faithfully the experimental conditions.

The observed double detachment yield contains series of peaks arising from resonances between the initial state of the transient atom and Rydberg series. In the range from 530 to 560 nm, the $1s2s$ state produced by photodetachment is coupled, via a two-photon transition, to Rydberg $1sns$ and $1snd$ states. In this case, we showed that double detachment proceeds through single detachment and (2 + 1) REMPI of the neutral. In the range from 685 to 730 nm, the $1s2p$ state of the atom is resonantly coupled by one photon to the $1s3s$ state and by two photons to the $1snp$ and $1snf$ Rydberg series. Double detachment proceeds in this case through single detachment and both (1 + 1 + 1) and (2 + 1) REMPI of the atom.

The influence of the laser polarization is manifest in the $1s2s$ case, where $1sns$ resonances disappear for circular polarization as a result of the dipole selection rules. Changes in the double detachment spectrum induced by different polarizations are further explained in terms of geometrical factors. In the $1s2p$ case, the magnetic quantum number M_f strongly influences double detachment and determines the ionization pathway in the neutral atom. Changing the polarization from linear to elliptical and circular substantially modifies the various M_f contributions, which could be computed with the theoretical model. Differences in the shape of the double detachment spectra are further explained by geometrical factors and the slight orientation of the atom produced by photodetachment. Finally, the sequential nature of double detachment was assessed by a two-laser experiment and no evidence of non-sequential processes was found.

The study of double detachment of He$^-$ in more intense laser fields is certainly of great interest since a comparison with lower intensities, where multiphoton processes dominate, is now possible. The present work could help disentangle sequential and nonsequential processes. Moreover, the influence of the magnetic quantum number M in strong field double detachment is expected to be important [8,9], and the present work provides a detailed understanding of this influence in the relatively low-intensity region. Finally, photoelectron spectroscopy of the present process could be a perspective for future work since it would provide additional information in terms of double detachment channels and angular distributions.

ACKNOWLEDGMENTS

This work was supported by the Fonds De La Recherche Scientifique - FNRS through IISN Grant Agreement No. 4.4504.10. Computational resources have been provided by the supercomputing facilities of the Université catholique de Louvain (CISM/UCL) and the Consortium des Équipements de Calcul Intensif en Fédération Wallonie Bruxelles (CÉCI)

TABLE I. Slater orbital parameters used to build the helium triplet state wave functions.

	$C_{jn\ell}$	$I_{jn\ell}$	$\zeta_{jn\ell}$		$C_{jn\ell}$	$I_{jn\ell}$	$\zeta_{jn\ell}$
$1s$	5.65685	1	2.00000	$2p$	0.25282	2	0.54467
$2s$	1.02331	1	1.57920	$3p$	0.14871	2	0.50810
	−0.33960	2	0.59932		−0.00928	3	0.31496
$3s$	0.51628	1	1.53349	$\bar{4}p$	5.69931	2	1.81486
	−0.18699	2	0.46220		−0.14792	3	0.88532
	0.02242	3	0.37501		0.00010	4	0.31256
$\bar{4}s$	3.72051	1	0.57067	$\bar{5}p$	7.08316	2	2.03268
	−23.34422	2	1.97582		−1.97318	3	0.90825
	7.95138	3	1.78719		0.75867	4	1.01816
	−1.16998	4	1.23540		−0.00003	5	0.35646
$\bar{5}s$	11.03473	1	1.17185	$3d$	0.00904	3	0.33361
	−24.98834	2	1.09440				
	15.71030	3	1.09465	$\bar{4}d$	1.20358	3	1.35014
	−3.08663	4	0.98350		−0.00025	4	0.36349
	0.46320	5	1.03562				
				$\bar{4}f$	0.57024	4	1.43379

TABLE II. Energies and excitation thresholds for the five lowest triplet states of helium. The theoretical values are compared with the accurate, nonrelativistic energies taken from Chap. 11 of Ref. [35] and the thresholds recommended by the National Institute of Standards and Technology (NIST) [34].

		Present (au)	Accurate (au)	Present (eV)	NIST (eV)
$1s2s$	2^3S	−2.17513	−2.17523	0.0	0.0
$1s2p$	2^3P^o	−2.13294	−2.13316	1.14805	1.14449
$1s3s$	3^3S	−2.06866	−2.06869	2.89720	2.89885
$1s3p$	3^3P^o	−2.05798	−2.05808	3.18754	3.18746
$1s3d$	3^3D	−2.05562	−2.05564	3.25203	3.25404

funded by the Fonds De La Recherche Scientifique - FNRS under Grant Agreement No. 2.5020.11, as well as by the Institut de Physique de Rennes.

APPENDIX: REDUCED DIPOLE MATRIX ELEMENTS FOR THE PHOTODETACHMENT OF He$^-$

The reduced dipole matrix elements $(\alpha_f L_f \ell L||\boldsymbol{D}||\alpha_i L_i)$ required when evaluating Eq. (3) for the partial cross sections were extracted from a standard R-matrix calculation. Here, we give details of this calculation, together with some illustrative results to assess the reliability of the reduced dipole matrix elements thus obtained.

In the R-matrix approach, configuration space is divided into two regions by a sphere encompassing the charge density of all states of the residual atom included in the calculation. Within this sphere, the states of the $(N+1)$-electron system are represented by a discrete set of antisymmetrized basis functions built from linear combinations of the residual atomic states coupled with a set of continuum orbitals representing the ejected electron, supplemented by a number of bound or short-range correlation configurations. The $(N+1)$-electron Hamiltonian is diagonalized in this basis, and the resulting eigenvalues and eigenvectors are used to construct the inverse logarithmic derivative matrix or R matrix on the boundary of the inner region. In the outer region, the ejected electron moves far from the target while the other electrons remain bound. Exchange between the ejected and bound electrons can then be neglected, so that the wave functions for the full system can be represented by a standard close-coupling expansion involving products of the residual atomic states and a set of unknown functions representing the ejected electron. These unknown functions satisfy an infinite set of coupled second-order differential equations, with the appropriate asymptotic boundary conditions determining if the solutions represent a bound state of the initial anion or a continuum state of the atom plus ejected electron. The initial bound state and final continuum states are then determined by matching the solutions in the inner and outer regions at their common boundary. For the initial bound state, this matching can only be performed at discrete energies, which are found by an iterative search algorithm.

Since the initial He$^-$ anion has a $^4P^o$ symmetry, after photodetachment the residual helium atom can only be left in a triplet state. The present calculation includes the five lowest triplet states of helium, whose wave functions were obtained using the CIV3 atomic structure computer code [44]. This code is based on a configuration interaction approach, in which the wave functions for a particular symmetry $|LS\pi\rangle$ are expressed as antisymmetric linear combinations of products of one-electron orbitals. In CIV3, the radial part of each orbital is written as a sum of Slater orbitals:

$$P_{n\ell}(r) = \sum_{j=1}^{k} C_{jn\ell} r^{I_{jn\ell}} \exp(-\zeta_{jn\ell} r). \tag{A1}$$

The coefficients $C_{jn\ell}$ are uniquely determined by orthonormality constraints if $k = n - \ell$, while the indices $I_{jn\ell}$ and the exponents $\zeta_{jn\ell}$ are variational parameters chosen to minimize the energies of particular atomic states.

The values of the parameters used in the current study are given in Table I. The $1s$ orbital is simply that for the hydrogenic He$^+$ ion. The $n = 2,3$ orbitals were all optimized

TABLE III. Oscillator strengths f and rates A in length (L) and velocity (V) forms for dipole allowed transitions involving the five lowest triplet states of helium, compared with the values recommended by NIST [34]. The figures in parentheses are the powers of ten by which the preceding number must be multiplied.

		f		A (sec^{-1})	
Transitions		Present	NIST	Present	NIST
$1s2s\,^3S$-$1s2p\,^3P^o$	L	0.5421	0.5394	0.1033 (8)	0.1022 (8)
	V	0.5320		0.1014 (8)	
$1s2s\,^3S$-$1s3p\,^3P^o$	L	0.5744 (−1)	0.6448 (−1)	0.8442 (7)	0.9475 (7)
	V	0.6378 (−1)		0.9373 (7)	
$1s2p\,^3P^o$-$1s3s\,^3S$	L	0.7019 (−1)	0.6951 (−1)	0.2795 (8)	0.2785 (8)
	V	0.6786 (−1)		0.2703 (8)	
$1s2p\,^3P^o$-$1s3d\,^3D$	L	0.6161	0.6102	0.7100 (8)	0.7070 (8)
	V	0.6085		0.7012 (8)	
$1s3s\,^3S$-$1s3p\,^3P^o$	L	0.9126	0.8914	0.1114 (7)	0.1074 (7)
	V	0.8693		0.1061 (7)	
$1s3p\,^3P^o$-$1s3d\,^3D$	L	0.1095	0.1120	0.1179 (5)	0.1292 (5)
	V	0.1055		0.1136 (5)	

on the associated $1snl$ state of helium. The pseudo-orbitals $\bar{4}s$ and $\bar{5}s$ were optimized on the $1s2s\ ^3S$ state, $\bar{4}d$ and $\bar{4}f$ on the $1s2p\ ^3P^o$ state. The $\bar{4}p$ and $\bar{5}p$ pseudo-orbitals were optimized on a linear combination of the $1s2p\ ^3P^o$ and $1s3p\ ^3P^o$ states as it was found that this gave the best energy separation between the two states.

The energies and excitation thresholds thus obtained are presented in Table II, where they are compared with those of a more accurate calculation [35] and with the values recommended by the National Institute of Standards and Technology (NIST). Oscillator strengths and transition probabilities are compared with the NIST values in Table III.

In the R-matrix calculation, the inner region extends out to $40\,a_0$, and 30 continuum orbitals per angular momentum ℓ are used to represent the ejected electron. The $(N+1)$-electron Hamiltonian in the inner region is diagonalized for the initial $^4P^o$ symmetry and the three final symmetries ^4S,^4P, ^4D allowed by the dipole selection rules. In the outer region, imposing decaying boundary conditions on the solutions of the coupled second-order differential equations in the $^4P^o$ symmetry yields an electron affinity of about 75.5 meV for the initial He^- state. This compares favorably with the value of 77.518 meV obtained by a more extensive calculation [39], the experimental value of 77.516 meV [39], and is slightly better than that of an earlier R-matrix calculation [11], in which the computed electron affinity was then slightly adjusted to agree with the accurate value. While such small differences may be important close to threshold, they have little effect on the overall cross sections in the range of photon wavelengths (500–800 nm) considered in this study, and we do not perform such an adjustment here. As shown in Fig. 11, presenting the total cross section for photodetachment of He^-, the agreement with the earlier work is very good [11].

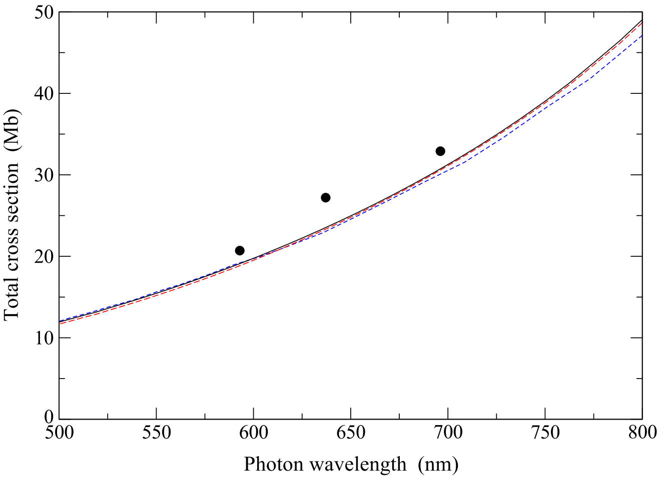

FIG. 11. Total cross section for the photodetachment of He^- as a function of the photon wavelength. Full line, R-matrix calculation using the length form of the dipole matrix elements; dashed line, R-matrix calculation using the velocity form of the dipole matrix elements; broken line, Ref. [11]; circles, experimental results from Ref. [13].

[1] T. Andersen, Phys. Rep. **394**, 157 (2004).

[2] H. Stapelfeldt and H. K. Haugen, Phys. Rev. Lett. **69**, 2638 (1992).

[3] H. Stapelfeldt, P. Kristensen, U. Ljungblad, T. Andersen, and H. K. Haugen, Phys. Rev. A **50**, 1618 (1994).

[4] V. V. Petrunin, J. D. Voldstad, P. Balling, P. Kristensen, T. Andersen, and H. K. Haugen, Phys. Rev. Lett. **75**, 1911 (1995).

[5] J. B. Greenwood, G. F. Collins, J. Pedregosa-Gutierrez, J. McKenna, A. Murphy, and J. T. Costello, J. Phys. B At. Mol. Opt. Phys. **36**, L235 (2003).

[6] J. Pedregosa-Gutierrez, P. A. Orr, J. B. Greenwood, A. Murphy, J. T. Costello, K. Zrost, T. Ergler, R. Moshammer, and J. Ullrich, Phys. Rev. Lett. **93**, 223001 (2004).

[7] B. Bergues, Y. Ni, H. Helm, and I. Y. Kiyan, Phys. Rev. Lett. **95**, 263002 (2005).

[8] H. W. van der Hart, Phys. Rev. A **74**, 053406 (2006).

[9] B. Bergues and I. Y. Kiyan, Phys. Rev. Lett. **100**, 143004 (2008).

[10] A. Gazibegović-Busuladžić, D. B. Milošević, W. Becker, B. Bergues, H. Hultgren, and I. Y. Kiyan, Phys. Rev. Lett. **104**, 103004 (2010).

[11] C. A. Ramsbottom and K. L. Bell, J. Phys. B At. Mol. Opt. Phys. **32**, 1315 (1999).

[12] J. Xi and C. F. Fischer, Phys. Rev. A **53**, 3169 (1996).

[13] D. J. Pegg, J. S. Thompson, J. Dellwo, R. N. Compton, and G. D. Alton, Phys. Rev. Lett. **64**, 278 (1990).

[14] F. Dunning and R. Stebbings, Phys. Rev. Lett. **32**, 1286 (1974).

[15] L. A. Lompré, G. Mainfray, B. Mathieu, G. Watel, M. Aymar, and M. Crance, J. Phys. B At. Mol. Phys. **13**, 1799 (1980).

[16] H. Haberland, M. Oschwald, and J. T. Broad, J. Phys. B At. Mol. Phys. **20**, 3367 (1987).

[17] H. Haberland and M. Oschwald, J. Phys. B At. Mol. Opt. Phys. **21**, 1183 (1988).

[18] M. Génévriez, X. Urbain, M. Brouri, A. P. O'Connor, K. M. Dunseath, and M. Terao-Dunseath, Phys. Rev. A **89**, 053430 (2014).

[19] P. Reinhed, A. Orbán, J. Werner, S. Rosén, R. D. Thomas, I. Kashperka, H. A. B. Johansson, D. Misra, L. Brännholm, M. Björkhage, H. Cederquist, and H. T. Schmidt, Phys. Rev. Lett. **103**, 213002 (2009).

[20] C. W. Walter, J. A. Seifert, and J. R. Peterson, Phys. Rev. A **50**, 2257 (1994).

[21] J. R. Peterson, Y. K. Bae, and D. L. Huestis, Phys. Rev. Lett. **55**, 692 (1985).

[22] P. A. Závodszky, L. Sarkadi, L. Víkor, and J. Pálinkás, Phys. Rev. A **50**, R899 (1994).

[23] M. Bylicki, J. Phys. B At. Mol. Opt. Phys. **30**, 189 (1997).

[24] D.-S. Kim, H.-L. Zhou, and S. T. Manson, Phys. Rev. A **55**, 414 (1997).

[25] C. A. Nicolaides and T. Mercouris, J. Phys. B At. Mol. Opt. Phys. **29**, 1151 (1996).

[26] P. G. Burke, *R-Matrix Theory of Atomic Collisions: Application to Atomic, Molecular, and Optical Processes*, Springer Series on Atomic, Optical, and Plasma Physics, Vol. 61 (Springer-Verlag, Berlin Heidelberg, 2011).

[27] A. M. Tumaikin and V. I. Yudin, Zh. Eksp. Teor. Fiz. **98**, 81 (1990) [Sov. Phys. JETP **71**, 43 (1990)].

[28] A. V. Taichenachev, A. M. Tumaikin, V. I. Yudin, and G. Nienhuis, Phys. Rev. A **69**, 033410 (2004).

[29] A. R. Edmonds, *Angular Momentum in Quantum Mechanics* (Princeton University Press, London, 1996).

[30] UK APAP (Atomic Processes for Astrophysical Plasmas network) [http://www.apap-network.org/] .

[31] J. P. Killingbeck and G. Jolicard, J. Phys. A. Math. Gen. **36**, R105 (2003).

[32] G. Jolicard and J. P. Killingbeck, J. Phys. A. Math. Gen. **36**, R411 (2003).

[33] P. Durand, Phys. Rev. A **28**, 3184 (1983).

[34] A. Kramida, Y. Ralchenko, J. Reader, and NIST ASD Team, NIST Atomic Spectra Database [http://www.nist.gov/pml/data/asd.cfm] .

[35] G. Drake, editor, *Springer Handbook of Atomic, Molecular, and Optical Physics* (Springer, New York, 2006), Vol. 1.

[36] B. W. Shore, *Multilevel Atoms and Incoherence*, The Theory of Coherent Atomic Excitation, Vol. 2 (Wiley, New York, 1990).

[37] H. C. Baker, Phys. Rev. A **30**, 773 (1984).

[38] R. B. Sidje, ACM Trans. Math. Softw. **24**, 130 (1998).

[39] P. Kristensen, U. V. Pedersen, V. V. Petrunin, T. Andersen, and K. T. Chung, Phys. Rev. A **55**, 978 (1997).

[40] T. E. Wall, D. B. Cassidy, and S. D. Hogan, Phys. Rev. A **90**, 053430 (2014).

[41] P. B. Corkum, Phys. Rev. Lett. **71**, 1994 (1993).

[42] K. C. Kulander, K. J. Schafer, and J. L. Krause, *Super-intense Laser-Atom Physics* (Plenum Press, New York, 1993).

[43] T. Brabec, M. Y. Ivanov, and P. B. Corkum, Phys. Rev. A **54**, R2551 (1996).

[44] A. Hibbert, Comput. Phys. Commun. **9**, 141 (1975).